

# Molecular imaging of tumor photoimmunotherapy: Evidence of photosensitized tumor necrosis and hemodynamic changes

**Kishimoto, Shun; Oshima, Nobu; Yamamoto, Kazutoshi; Munasinghe, Jeeva; Ardenkjær-Larsen, Jan Henrik; Mitchell, James B.; Choyke, Peter L.; Krishna, Murali C.**

*Published in:*
Free Radical Biology and Medicine

*Link to article, DOI:*
10.1016/j.freeradbiomed.2017.12.034

*Publication date:*
2018

*Document Version*
Peer reviewed version

HHS Public Access

Author manuscript

*Free Radic Biol Med*. Author manuscript; available in PMC 2019 February 20.

Published in final edited form as:

*Free Radic Biol Med*. 2018 February 20; 116: 1–10. doi:10.1016/j.freeradbiomed.2017.12.034.

# Molecular imaging of tumor photoimmunotherapy: Evidence of photosensitized tumor necrosis and hemodynamic changes

**Shun Kishimoto**[1], **Nobu Oshima**[2], **Kazutoshi Yamamoto**[1], **Jeeva Munasinghe**[3], **Jan Henrik Ardenkjaer-Larsen**[4], **James B. Mitchell**[1], **Peter L. Choyke**[5], and **Murali C. Krishna**[1]

[1]Radiation Biology Branch, Center for Cancer Research, National Cancer Institute, NIH, Bethesda, MD 20892

[2]Urologic Oncology Branch, Center for Cancer Research, National Cancer Institute, NIH, Bethesda, MD 20892

[3]Mouse Imaging Facility, National Institute of Neurological Disease and Stroke, NIH, Bethesda, MD 20892

[4]Center for Magnetic Resonance, Denmark Technical University, Copenhagen, Denmark

[5]Molecular Imaging Program, Center for Cancer Research, National Cancer Institute, NIH, Bethesda, MD 20892

## Abstract

Near-infrared photoimmunotherapy (NIR PIT) employs the photoabsorbing dye IR700 conjugated to antibodies specific for cell surface epidermal growth factor receptor (EGFR). NIR PIT has shown highly selective cytotoxicity *in vitro* and *in vivo*. Cell necrosis is thought to be the main mode of cytotoxicity based mainly on *in vitro* studies. To better understand the acute effects of NIR PIT, molecular imaging studies were performed to assess its cellular and vascular effects.

In addition to *in vitro* studies for cytotoxicity of NIR PIT, the *in vivo* tumoricidal effects and hemodynamic changes induced by NIR PIT were evaluated by $^{13}C$ MRI using hyperpolarized [1,4-$^{13}C_2$] fumarate, $R_2$* mapping from $T_2$*-weighted MRI, and photoacoustic imaging. *In vitro* studies confirmed that NIR PIT resulted in rapid cell death via membrane damage, with evidence for rapid cell expansion followed by membrane rupture. Following NIR PIT, metabolic MRI using hyperpolarized fumarate showed the production of malate in EGFR-expressing A431 tumor xenografts, providing direct evidence for photosensitized tumor necrosis induced by NIR PIT. $R_2$* mapping studies showed temporal changes in oxygenation, with an accompanying increase of deoxyhemoglobin at the start of light exposure followed by a sustained decrease after cessation of light exposure. This result suggests a rapid decrease of blood flow in EGFR-expressing A431 tumor xenografts, which is supported by the results of the photoacoustic imaging experiments. Our

Address correspondence to: Murali K. Cherukuri, Ph.D., Radiation Biology Branch, National Cancer Institute, Bldg. 10, Room B3-B69, Bethesda, MD 20892, Phone: (301) 451-6752, Fax: (301) 480-2238, cherukum@mail.nih.gov.



Conflict of Interest: No potential conflicts of interest were disclosed.

findings suggest NIR PIT mediates necrosis and hemodynamic changes in tumors by photosensitized oxidation pathways and that these imaging modalities, once translated, may be useful in monitoring clinical treatment response.

## graphical abstract

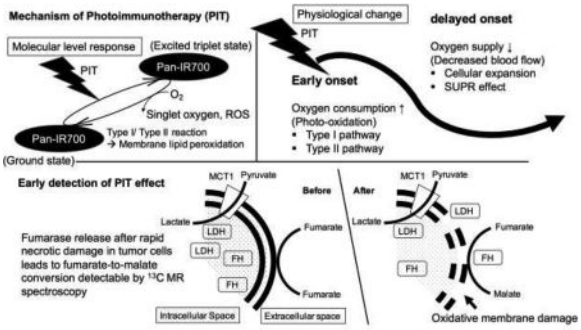


### Keywords

Photoimmunotherapy; $^{13}C$ MRI; Photoacoustic Imaging; Hemodynamic Change

## Introduction

Photodynamic therapy (PDT) is a well-known cancer treatment modality in which a visible light-absorbing chromophore or photosensitizer (PS) is administered intravenously followed by selective irradiation of the tumor with visible light [1]. The PS accumulates preferentially in the tumor via the enhanced permeability and retention (EPR) effect.

The clinical application of PDT is limited for several reasons. Selective illumination of the tumor not only results in tumor killing but can also cause damage to adjacent normal tissue [1–3]. In addition, the patient remains light-sensitive after exposure to the PS. Finally, the photochemical mechanisms underlying PDT are thought to be mediated by free radicals and singlet oxygen.

$$^1PS_g \rightarrow {}^1PS_e \quad (1)$$

$$^1PS_e \rightarrow {}^3PS_e \quad (2)$$

$$^3PS_e + {}^3O_2 \rightarrow PS + {}^1O_2(\text{Type II}) \quad (3)(\text{Energy transfer})$$

$$\text{or } {}^3PS_e + LH \rightarrow L^{\cdot} + PS^{\cdot -}(\text{Type I}) \quad (4)(\text{Electron transfer})$$

Where $PS_g$ and $PS_e$ are ground state and excited state of photosensitizer, respectively. $^1PS_g$ is excited to $^1PS_e$ by irradiating light (1), which then transits to $^3PS_e$ via intersystem crossing (2). Energy transfer results in generation of singlet oxygen in type II reaction (3), whereas electron transfer results in generation of free radical in type I reaction (4). Free radicals generated through Type I photochemical mechanisms by the PS can lead to membrane lipid peroxidation, while singlet oxygen generated by a Type II mechanism adds

across double bonds of membrane lipids [5–7]. Oxidative stress supported by Type I and Type II mechanisms cause membrane damage [6]. Thus, while PDT is used in selected cases, it is still not widely applicable in cancer treatment [1, 4].

In contrast to PDT, which uses a non-targeted PS, in near-infrared photoimmunotherapy (NIR PIT), PSs are covalently linked to an antibody to provide tumor selectivity [8, 9]. The highly hydrophilic PS, IR700, when conjugated to an antibody targeting cell membrane receptors expressed in tumors, can accumulate selectively at doses able to induce phototoxic effects [8–10]. For example, using an anti-epidermal growth factor receptor (EGFR) monoclonal antibody (mAb) conjugated to IR700, NIR PIT demonstrated potent and selective cytotoxic effects immediately after light exposure in tumor xenografts and in spontaneous EGFR-expressing cancer, resulting in dramatic reductions in tumor size [11–13]. *In vitro*, cells exhibited rapid swelling and membrane rupture, indicating a necrotic mechanism. Systematic studies showed that: a) tumor killing was dependent on IR700-Ab dose and light exposure; b) in targeting the EGFR receptor, panitumumab was superior to cetuximab; c) multiple NIR PIT cycles proved superior to a single treatment; and d) antibody fragments were as efficacious as whole antibodies [14–17].

NIR PIT studies also showed a nearly immediate increase in vascular permeability that facilitated the delivery of intravenous therapeutics, such as liposomal encapsulated doxorubicin, resulting in a synergy between NIR PIT and chemotherapy [18–20]. More recent studies have shown that NIR PIT can be used to target the immunosuppressive Treg cells which help cancer cells evade the normal immune response. This not only causes regression in treated tumors but also leads to responses in untreated tumors, opening avenues for incorporating this modality in cancer immunotherapy [21, 22].

Several imaging techniques have been used to monitor the effects of NIR PIT. Bioluminescence imaging and fluorescence lifetime imaging have been used to follow treatment responses preclinically [23, 24]. Clinically translatable imaging techniques include positron emission tomography (PET) with $^{18}$F-fludeoxyglucose ([$^{18}$F]FDG) uptake, magnetic resonance imaging (MRI) measuring changes in T1, measurement of the apparent diffusion coefficient (ADC), and detection of macromolecular contrast agent uptake, all of which showed early profound changes [19, 25]. For instance, [$^{18}$F]FDG uptake was found to be significantly reduced immediately following NIR PIT, suggesting that this treatment modality causes rapid cytotoxicity [25]. However, *in vivo* imaging of cell necrosis and related hemodynamic changes have been lacking, but would potentially be useful for treatment monitoring.

Cell necrosis and EPR are considered hallmarks of NIR PIT. Biomarkers that can detect these endpoints would be useful in a clinical setting to monitor the response to NIR PIT. $^{13}$C-labeled fumarate, a substrate for fumarate hydratase (FH), can be hyperpolarized for MRI and used to non-invasively image necrotic death [26, 27]. Fumarate is converted to malate by FH, which is an intracellular enzyme. Fumarate is cell-impermeable and remains unmodified in intact tissue. Upon the rapid necrotic cell death seen following NIR PIT, we hypothesized that FH would leak out and convert fumarate to malate in the extracellular milieu. Blood flow and blood oxygenation can also be monitored by $T_2$*-weighted MRI and

photoacoustic imaging (PAI), as these methods are influenced by deoxyhemoglobin and oxyhemoglobin, respectively [28–30]. The current study evaluates these imaging techniques to monitor therapeutic responses to NIR PIT *in vivo*.

## Materials and Methods

### Animals, tumor model, and PIT

All animal experiments were performed in compliance with the Guide for the Care and Use of Laboratory Animal Resources (National Research Council, 2011) and were approved by the NCI Animal Care and Use Committee. Female athymic nude mice were supplied by the Frederick National Laboratory for Cancer Research (Frederick, MD). A431 and H520 cell lines were purchased from the American Type Culture Collection (Manassas, VA). A431 and H520 solid tumors were formed by injecting $2 \times 10^6$ cells and $5 \times 10^6$ cells, respectively, subcutaneously into the right hind legs of mice. The tumor volume was calculated by using the formula for a prolate ellipsoid: length × width × depth × ½. The growth of A431 tumors (n = 5 for both control groups and PIT-treated groups) was monitored from when the tumor volume was approximately 200 $mm^3$ to a volume of 1500 $mm^3$. Mice were treated with PIT once at day 4 after tumor cells injection. During MRI and PAI measurements, the mouse breathing rate was monitored with a pressure transducer (SA Instruments Inc.) and was maintained at 80 ± 10 breaths per minute. Core body temperature was also monitored with a nonmagnetic rectal temperature probe (FISO, Québec, Canada) and was maintained at 36 ± 1°C.

Panitumumab-IR700 (Pan-IR700) was prepared using previously described methods [11]. For the *in vitro* study, cells were incubated with 12.5 μg/mL Pan-IR700 for 30 min, washed with PBS three times, and then exposed to NIR light illumination with infrared NIR LED laser at a wavelength of 690 nm (5 $J/cm^2$). The cells were then washed with PBS three times and evaluated by flow cytometry. For *in vivo* studies, 24 h prior to PIT treatment, tumor-bearing mice were pretreated with 200 μg of Pan-IR700 (i.p.). For $T_2$*-weighted MRI and PAI experiments, the NIR light was delivered using a fiberoptic cable coupled with an LED laser (36 $J/cm^2$). For $^{13}C$ MRI experiments and tumor growth experiments, the same LED laser was used (200 $J/cm^2$).

### In vivo fluorescence imaging studies

Both A431 and H520 tumors were studied after they reached volumes of approximately 300 $mm^3$. Fluorescence images of Pan-IR700 were obtained with a fluorescence camera (Carestream, Carestream Health, Inc., NY) using a 690 nm excitation and 750 nm emission filters 24 h after i.p. injection of 200 μg of Pan-IR700. The fluorescence images were then overlaid on X-ray images of each mouse. The scale of signal detection is indicated in Figure 1B.

### Flow cytometry analysis

The affinity of tumor cells for Pan-IR700 was assessed by incubating cells ($5 \times 10^6$) with or without Pan-IR700 on ice for 1 h followed by three washings in Dulbecco's PBS (DPBS) + 1% fetal bovine serum (FBS). PIT-induced lipid peroxidation was assessed by incubating

PIT-treated cells with rabbit anti-4-hydroxy-2-nonenal (4-HNE) Michael Adducts polyclonal antibody for 30 min on ice (1:250; EMD Millipore, Billerica, MA), followed by three washings in DPBS + 1% FBS and incubation with Alexa Fluor-conjugated goat anti-rabbit secondary antibody (1:250; Thermo Fisher Scientific Inc., Waltham, MA) for 1 h on ice. Following staining, the cell fluorescence was measured by flow cytometry (FACSCALIBUR, BD Biosciences, San Jose, CA).

### Histostaining

Tumor-bearing mice were euthanized, and tumor tissues were removed from mice. Tumor tissues were frozen in OTC compound (SAKURA) using ultracold ethanol. Frozen tumors were sectioned to 10 mm thick using a cryostat, and the sections were thaw-mounted on glass slides. After fixed with 4% paraformaldehyde, sections were stained with hematoxylin and eosin and mounted on permount for histological observation.

### FH enzyme activity assay

A serum sample was obtained from untreated mice and from NIR PIT-treated mice 1, 3, 6, 12, 24 h after treatment (n = 3 in each group) and FH activity was measured with Fumarase Specific Activity Assay Kit (Abcam, Cambridge, MA) in accordance with the manufacturer's instruction manual.

### MRI experiments for $R_2$* mapping and hyperpolarized $^{13}C$ spectroscopy

The MRI experiments were initiated when the tumors were approximately 200–300 $mm^3$. For $T_2$*, and $R_2$* mapping study, multiple gradient echo magnetic resonance images were acquired on a 9.4 Tesla MRI scanner (Bruker Biospin, Billerica, MA). The repetition time (TR), echo time (TE), number of average, flip angle, slice thickness, and field of view (FOV) were set to 312.5 ms, 7 ms, 1, 30 °, 3.2 mm, and 32 × 64 pixels (16 mm × 32 mm), respectively. For $R_2$* measurements, images with multiple TE values (2, 7, 12, 17 and 22 ms for A431 tumors; and 2, 7, and 12 ms for H520 tumors) were used for calculation of $T_2$* and $R_2$* mapping. For $^{13}C$ study, [1-$^{13}C$] pyruvic acid (30 mL) or [1,4-$^{13}C_2$] fumaric acid (2.5 M in 30 mL deuterated DMSO), containing 15 mM Oxo63 and 2.5 mmol/L gadolinium chelate ProHance (Bracco Diagnostics, Monroe Township, NJ), was hyperpolarized using the Hypersense DNP polarizer (Oxford Instruments, Abingdon, UK) as described previously [32]. After the polarization reached 80% of the plateau value, the hyperpolarized sample was rapidly dissolved in 4.5 mL of a superheated alkaline buffer that consisted of 40 mmol/L HEPES, NaOH, and 100 mg/L EDTA. A hyperpolarized [1-$^{13}C$] pyruvate or [1,4-$^{13}C2$] fumarate solution (96 mmol/L and 16.7 mmol/L, respectively) was rapidly injected intravenously through a catheter placed in the tail vein of the mouse (12 mL/g body weight). The dynamic spectrum was taken from a 3 Tesla dedicated MR Solutions animal scanner (MR SOLUTIONS Ltd., Boston, MA) using a 17-mm home-built $^{13}C$ solenoid coil placed inside of a saddle coil for $^{1}H$. The right leg with tumor implant was placed in the middle of the dual coil for data acquisition. During the scan, mice were anesthetized using isoflurane (1.5–2.5 %). Respiration was continuously monitored to ensure the animal well- being and and data reproducibility. Both 1H and 13C are tuned and matched and anatomical image was taken after shimed on proton. $^{13}C$ spectra for [1-$^{13}C$] pyruvate injection were acquired every 1 sec for 240 sec from the whole leg including each tumor (n = 4 for control and n = 3 for

irradiated group). $^{13}C$ spectra following hyperpolarized [1,4-$^{13}C_2$] fumarate injection were acquired for 180 sec in the same manner (n = 3 for control and n = 4 for irradiated group). The repetition time, spectral width, flip angle, and number of average were 1000 ms, 3300 Hz, 10 °, and 1, respectively.

### Photoacoustic imaging experiments

Tumors were imaged with the VisualSonics Vevo®LAZR System (FUJIFILM VisualSonics Inc., Canada) using a 21-MHz linear array transducer system (central frequency) integrated with a tunable nanosecond pulsed laser. The system was calibrated by the manufacturer before initiating data acquisition. Mice were anesthetized with isoflurane (1.5–2.5%) and raspiration and temperature were continuously monitored in the same manner as MR studies. The tumor area in the sagittal plane of the leg was determined manually from concurrently acquired ultrasound images. In this study, the experiments were performed on a fixed plane depicting the middle of the tumor in order to achieve better temporal resolution. For $O_2$ status assessments, photoacoustic images in the tumor area were collected with OxyHemo-Mode (wavelength 750nm/850nm) every 1 sec for 10 min. Oxygen saturation of hemoglobin ($sO_2$) and total hemoglobin values in the tumor area were calculated using OxyZatet™ tool based on a previously reported and tested algorithm [31]. For a noise control, threshold of total hemoglobin in relation to the maximum possibly leval was set to 20% for all experiments as this was found to be empirically reasonable value. Values below the threshold was discarded and appear black in all images.

### Data analysis

MRI data were analyzed using MATLAB (MathWorks), ImageJ 1.49v (NIH), and Paravision 5.1 (Bruker). $R_2$* maps were derived by linear regression of log(MR signal intensity) for each pixel. Statistical analyses were carried out using R statistical software (https://www.rproject.org/). Statistical significance was considered to be at the $P<0.05$ level. All results are expressed as mean ± standard deviation. Welch's t-test was performed to evaluate the statistical difference between the groups. A log-rank test was performed for Kaplan Meier survival curves.

## Results

### Affinity of Pan-IR700 for EGFR-expressing cells

Two cell lines were used in these experiments: A431, which is a highly EGFR-positive tumor cell line, and H520, which does not express EGFR and served as a negative control. Panitumumab is a fully humanized IgG2 mAb directed against EGFR while cetuximab is a chimeric (mouse/human) mAb. The evaluation of PIT efficacy of both panitumumab-IR700 (Pan-IR700: panitumumab covalently linked with IR700) and cetuximub-IR700 was performed by Sato.et al [16]. In their study, Pan-IR700 showed higher treatment efficacy due to its lower hepatic catabolism. Thus, in this study, we used Pan-IR700 for the evaluation of PIT treatment efficacy.

The binding affinity of each cell line was assessed after incubation with Pan-IR700 (12.5 μM) for 30 min on ice, followed by washing and flow cytometry (Figure 1A). There was no

difference in the cytometric profiles of the unexposed versus Pan-IR700-treated H520 cells (Figure 1A, top), whereas there was a considerable difference in the cytometric profiles of unexposed versus Pan-IR700-treated A431 cells (Figure 1A, bottom). *In vivo* xenografts of A431 and H520 cells showed marked differences in fluorescence after administration of Pan-IR700. Figure 1B shows the fluorescence optical image overlaid on the corresponding X-ray image taken from A431 and H520 tumor-bearing mice 24 h after pretreatment with Pan-IR700. High target accumulation of Pan-IR700 was shown in the A431 tumor xenografts, but not in the H520 tumor xenografts. These *in vitro* and *in vivo* binding studies confirm the strong binding affinity of the Pan-IR700 immunoconjugate for the EGFR-expressing tumor cells.

## Anti-tumor effects of NIR PIT

The cytotoxic effects of PIT using Pan-IR700 were tested in A431 and H520 cells *in vitro* using flow cytometry. Figures 2A, B (top row) show the histograms of forward scatter analysis, which is sensitive to the sizes of NIR PIT-treated (red) and untreated (black) cells. The results indicate that only the EGFR-expressing A431 cells showed morphological changes after NIR PIT, as indicated by a right shift. On the other hand, the H520 cells treated with NIR PIT under identical conditions had no observable effects. Figures 2C, D (bottom row) show the histograms of the same cells stained with 4-HNE antibody, which detects products formed via lipid peroxidation. These results suggest that only EGFR-expressing cells were susceptible to NIR PIT-mediated cytotoxicity, resulting in oxidative membrane damage.

The *in vivo* effects of NIR PIT on A431 and H520 xenografts pretreated with Pan-IR700 were assessed following exposure to a 690 nm LED laser (200 J/cm$^2$). The A431 and H520 tumor specimens were dissected from animals immediately after NIR PIT. Figure 3A shows the H&E stained tissue sections of both untreated and NIR PIT-treated A431 and H520 tumors. While the untreated and NIR PIT-treated H520 cells showed no morphological differences, the A431 cells treated with NIR PIT showed cellular expansion and regions with cell membrane rupture (Figure 3A, arrow in right bottom panel). Tumor growth rates were also measured for A431 tumors with and without NIR PIT treatment, and the results are shown as tumor growth kinetics (Figure 3B) and Kaplan-Meier survival curves (Figure 3C). The results show that while the control (no Pan-IR700) mice and mice receiving only Pan-IR700 showed no effects, the group that received Pan-IR700 and NIR PIT (200 J/cm$^2$) (filled squares) showed significant alterations in tumor growth and statistically significantly prolonged survival ($p = 0.001$). For instance, at the level of 50% survival, the NIR PIT treatment group showed a 1.44-fold prolongation of survival time.

## Hyperpolarized $^{13}$C MRI detecting treatment response after NIR PIT

Necrotic cell death can be directly and non-invasively monitored by hyperpolarized MRI using $^{13}$C-labeled fumarate as a reporter. Fumarate is cell impermeable and therefore does not get converted to malate by FH, which is strictly intracellular in intact cells. However, in necrotic cells FH is released into the tumor bed immediately after necrosis and can convert fumarate to malate (Figure 4A). This phenomenon can be imaged by $^{13}$C MRI following injection of hyperpolarized [1,4-$^{13}C_2$] fumarate into treated and untreated mice, an approach

which was successfully shown to report on necrotic cell death in tumor xenografts treated with etoposide or in acute kidney injury [26, 27, 33]. The balance between apoptosis and necrosis induced by PDT depends on the type and dosage of photosensitizer. However, in case of PIT, due to high affinity of Pan-IR700 with EGFR, high level of accumulation of Pan-IR700 to cellular membrane is achieved, leading to acute necrotic cell death induced by the strong oxidative damage to cellular membrane. In this study, non-localized 1D spectral signal from tumor implanted leg was acquired continuously for 180 seconds after hyperpolarized [1,4-$^{13}C_2$] fumarate injection and the conversion of fumarate to malate was quantitatively assessed. We examined untreated and NIR PIT-treated mice with hyperpolarized MRI following administration of fumarate 1 h after NIR PIT, and the results are shown in Figure 4B. The untreated mice with A431 tumors showed no evidence of conversion of fumarate to malate while NIR PIT-treated mice with A431 tumors showed detectable malate production (Figure 4B), supporting necrotic cell death as a mechanism in NIR PIT. The malate to fumarate ratio was significantly different only in NIR PIT-treated mice ($p = 0.02$ at 30 sec after injection) (Figure 4C). To examine the release profile of FH following NIR PIT as an indicator of necrotic cell death, serum activity of this enzyme were determined (Figure 4D). FH levels were observed to increase following NIR PIT, reaching a peak at 6 h after treatment ($p = 0.004$ versus no treatment). These results suggest that FH activity may be a useful surrogate marker to monitor NIR PIT efficacy.

Hyperpolarized MRI has also been used to monitor response in tumor xenografts after treatment with anti-proliferative therapies such as doxorubicin and ionizing radiation using [1-$^{13}$C] pyruvate administration [34, 35]. Tumor cells *in vitro* and *in vivo* exhibit high levels of aerobic glycolysis, which reflects a metabolic shift involving the conversion of pyruvate to lactate to generate energy (the Warburg phenomenon) [36]. A reduction in the conversion of pyruvate to lactate after anti-proliferative treatment in tumors can be associated with DNA damage, depletion of the NAD(P)H coenzyme pool, loss of lactate dehydrogenase (LDH) activity, and decreased cellularity. However, the conversion of pyruvate to lactate depends on LDH that is both intra- and extracellular. Thus, it was anticipated that NIR PIT would have no effect on conversion of pyruvate to lactate. Hyperpolarized $^{13}$C-MRI studies in A431 tumor xenografts monitoring the conversion of pyruvate to lactate in control (untreated) or NIR PIT-treated mice showed no significant difference (Figure 4E), suggesting that the cell death induced by NIR PIT is markedly different compared to DNA damaging chemotherapeutic agents or ionizing radiation. Figure 4A schematically summarizes the results obtained from $^{13}$C MRI using hyperpolarized fumarate and pyruvate to monitor necrotic or metabolic changes following NIR PIT in A431 xenografts.

### Assessment of treatment response during NIR PIT by $T_2$*-weighted MRI

In a recent study, Sano et al. demonstrated that super-enhanced permeability and retention was induced by NIR PIT in tumors [20, 37]. This PIT-induced effect in tumor vasculature was exploited to deliver increased doses of nano-encapsulated chemotherapeutics such as doxorubicin to achieve improved therapeutic effects. We conducted continuous $T_2$*-weighted MRI with multiple TE values in the EGFR-expressing A431 tumor xenografts and the control H520 tumors following NIR PIT plus pre-treatment with Pan-IR700 to evaluate the hemodynamic changes. A set of images with multiple TE values is used to obtain $T_2$*

and $R_2$* maps and these mapes are acquired continuously for 600 seconds. Figure 5A shows the experimental protocol with four groups of tumor-bearing mice in this experiment (NIR applied group and NIR applied after Pan-IR700 treatment group for both H520 tumor and A431 tumor). Pan-IR700 (200 μg) was administered for localization. After 24 h, 36 J/cm$^2$ of NIR illumination (wavelength 690 nm) was applied to the surface of the tumor of all groups using a fiberoptic cable coupled with an LED laser setup during the MRI acquisition. $T_2$*-weighted scans were carried out prior to (0–2 minutes), during (2–5 minutes), and after (5–10 minutes) NIR exposure. Figure 5B shows the anatomic image followed by representative maps of the percentage change in $T_2$*-weighted signal intensity before (2 min), immediately after NIR exposure (5 min), and at recovery (10 min post NIR exposure) in the H520 tumor xenograft (top row) and the A431 xenograft (bottom row). Change in $R_2$* in the tumor area was plotted for A431 and H520 tumor xenografts treated with NIR but without Pan-IR700 or administered with Pan-IR700 24 h prior to treatment (Figure 5C). $R_2$* in the tumor area was plotted in this study because $T_2$*-weighted signals can be affected by flow effects (T1 contrast). The $R_2$* plot for the NIR PIT-treated A431 group showed a sharp rise immediately after the start of NIR PIT, followed by a significant decrease, which suggests a biphasic deoxyhemoglobin level change (Figure 5C, bottom). The $R_2$* plot for A431 tumors without Pan-IR700 pre-administration showed only a gradual increase during NIR exposure, followed by a gradual return to near-baseline. This change is suggestive of increased deoxyhemoglobin levels delivered to dilated blood vessel due to heating by NIR exposure. Compared to the A431 tumors, modest dynamic changes were observed in the $R_2$* maps of the H520 tumors.

### Assessment of treatment response during NIR PIT by photoacoustic imaging (PAI)

PAI provides a dynamic assessment of changes in oxyhemoglobin and total hemoglobin with an anatomic overlay in live organisms by spectral measurement of hemoglobin at 750 nm and 850 nm. For a better understanding of the physiological changes monitored by MRI, which were attributed to $R_2$* changes in the NIR PIT experiments with A431 tumor xenografts, we conducted PAI in the A431 and H520 xenografts in mice treated with Pan-IR700. Results from before, during, and after NIR exposure are shown in Figure 6. The experimental protocol used for these experiments was identical to that used for the MRI experiments (Figure 5A). The NIR light exposure conditions were also the same as for the MRI experiments. Figure 6A shows the anatomic image (B mode) followed by PAI before (0–2 min), immediately after NIR exposure (5 min), and at recovery (10 min post-NIR exposure) in representative H520 tumor xenografts (top row) and A431 xenografts (bottom row). The results from these images of the tumor region are quantified as oxygen saturation of hemoglobin ($sO_2$) and total hemoglobin concentration and plotted in Figure 6B. Almost no change in $sO_2$ and a weak increase in hemoglobin concentration were observed during the NIR PIT in H520 tumors. To the contrary, A431 tumors showed a rapid drop in $sO_2$ accompanied by a drop in total hemoglobin, suggesting a marked reduction in blood volume. These changes agree with the $R_2$* changes, suggesting increased deoxyhemoglobin, a consequence of lower $sO_2$. The weak but non-significant increase in total hemoglobin in H520 tumors may be a result of vasodilation caused by mild heating from light exposure. The abrupt drop in $sO_2$ and total hemoglobin in A431 tumors treated with NIR PIT was in agreement with the drop in blood flow from previous studies [38].

## Discussion

Recently developed photo-immunoconjugates using IR700 rely on the hydrophilic nature of this fluorophore and its ability to conjugate to targeted antibodies without changing the pharmacokinetics of the native macromolecule [12, 39]. Proposed mechanisms of phototoxicity include direct photochemical damage as well as photo-oxidation [40]. Experimental data suggest that at low radiant flux, photocatalytic reactions that conserve the chromophore and generate reactive oxygen species (ROS) may underlie PIT's effects [40]. At higher radiant flux, generally a characteristic of dye bleaching experiments [41], direct phototoxicity independent of $O_2$ or ROS may play a dominant role [11]. Similarly, in co-culture experiments, only targeted cells displayed cytotoxicity whereas adjacent untargeted cells with access to ROS were unaffected, suggesting that direct effects may have a significant contribution [42]. In this study, *in vitro* membrane damage following cell expansion was observed only in A431 cells by flowcytometric analysis (Figure 2B and 2D). *In vivo* studies of A431 cells using Pan-IR700 are described in previous reports. NIR light (wavelength 690 nm) exposure induces immediate cytotoxic effects and eventually leads to tumor shrinkage [24]. The IR700 covalently linked in the hydrophilic region of the antibody confers multiple modes of damage in the Pan-IR700 molecule, which can support direct photochemical damage as well as contributions from photo-oxidation reactions. *In vitro* and *in vivo* studies confirmed that cell surface receptors for panitumumab and light exposure are necessary to elicit membrane damage leading to cell death *in vitro* [42]. A recent study examined imaging biomarkers in tumors treated with NIR PIT using Pan-IR700 [19]. MRI 1–2 h after PIT in tumor-bearing mice showed increased $T_2$* with an accompanying decrease in ADC within treated tumors. These observations suggest that PIT induced tumor edema, which can increase $T_2$* values, while membrane rupture followed by extrusion of cellular contents results in increasing tumor viscosity and decreased ADC values in the tumor microenvironment immediately after treatment. Additional imaging studies showed that NIR PIT in combination with Pan-IR700 results in enhanced permeability, vessel dilation, blood pooling, and reduced blood flow [18–20, 38]. Considering the temporal changes we observed in serum FH and our histology data, PIT exerts its effects immediately after the treatment but needs a few hours for FH to be released into the systemic circulation.

The conversion of hyperpolarized [1,4-$^{13}C_2$] fumarate to malate in NIR PIT-treated A431 tumor xenografts strongly suggests necrosis as a mechanism of cell death. Serum fumarate levels showed a peak 6 h post-PIT. These results provide direct support to previous studies suggesting tumor necrosis as the major effect of NIR PIT. Attenuated conversion of [1-$^{13}$C] pyruvate to lactate is an established biomarker of treatment response in tumors when using DNA damaging treatments such as ionizing radiation or chemotherapeutic drugs [34, 35] that lead to metabolic death. The lack of change in pyruvate to lactate conversion in our assays suggests that the cause of cell death after NIR PIT is not metabolic but rather necrotic,.

It has been previously demonstrated that NIR PIT causes marked increases in permeability and retention of macromolecules [20]. It is proposed that the perivascular tumor destruction caused by NIR PIT leads to vascular resistance and leakage of serum into the tumor [18, 43]. This effect can be observed for up to 8 h after NIR PIT. Marked MRI signal intensity

changes were seen in NIR PIT-treated A431 tumors, with an accompanying increase in $R_2$* during light exposure, suggesting that PIT induces a rapid accumulation of deoxyhemoglobin which may be associated with oxygen consumption. The sustained decrease in $R_2$* after light exposure is consistent with earlier results in which decreased blood flow after PIT was observed. The decrease in $sO_2$ and a decrease in total hemoglobin in A431 tumors detected by PAI (and not seen in H520 tumors treated with NIR PIT) suggests that NIR PIT is accompanied initially by rapid oxygen consumption and/or rapid drop in blood flow.

In conclusion, our study shows that the therapeutic effects of NIR PIT with Pan IR700 in EGFR expressing tumors can be monitored by imaging techniques such as hyperpolarized $^{13}C$ MRI, BOLD MRI, and PAI. This study elucidated the early metabolic and hemodynamic changes induced by NIR PIT using several clinically applicable imaging techniques whose results were corroborated by $sO_2$ measurements and total hemoglobin changes acquired from PAI. The results provide direct evidence of the comprehensive tumoricidal effects of NIR PIT, including necrotic cell death mediated by photo-oxidation processes and dramatic hemodynamic changes, which suggests a unique mechanism of cancer cell death compared to standard therapies.

## Acknowledgments

This research was supported by the Intramural Research Program of the Center of Cancer Research, National Cancer Institute, National Institutes of Health.

## References

1. Dougherty TJ. Photodynamic therapy (PDT) of malignant tumors. Crit Rev Oncol Hematol. 1984; 2:83–116. [PubMed: 6397270]
2. Levy JG. Photodynamic therapy. Trends Biotechnol. 1995; 13(1):14–8. [PubMed: 7765800]
3. Roberts WG, Hasan T. Tumor-secreted vascular permeability factor/vascular endothelial growth factor influences photosensitizer uptake. Cancer Res. 1993; 53:153–7. [PubMed: 8416739]
4. Mitchell JB, McPherson S, DeGraff W, Gamson J, Zabell A, Russo A. Oxygen dependence of hematoporphyrin derivative-induced photoinactivation of Chinese hamster cells. Cancer Res. 1985; 45:2008–11. [PubMed: 3157442]
5. Agostinis P, Berg K, Cengel KA, Foster TH, Girotti AW, Gollnick SO. Photodynamic therapy of cancer: an update. CA Cancer J Clin. 2011; 61:250–81. [PubMed: 21617154]
6. Girotti AW. Photosensitized oxidation of membrane lipids: reaction pathways, cytotoxic effects, and cytoprotective mechanisms. J Photochem Photobiol B. 2001; 63:103–13. [PubMed: 11684457]
7. Kessel D. Death pathways associated with photodynamic therapy. Med Laser Appl. 2006; 21:219–24. [PubMed: 19890442]
8. Pogrebniak HW, Matthews W, Black C, Russo A, Mitchell JB, Smith P. Targetted phototherapy with sensitizer-monoclonal antibody conjugate and light. Surg Oncol. 1993; 2:31–42.
9. Oseroff AR, Ohuoha D, Hasan T, Bommer JC, Yarmush ML. Antibody-targeted photolysis: selective photodestruction of human T-cell leukemia cells using monoclonal antibody-chlorin e6 conjugates. Proc Natl Acad Sci U S A. 1986; 83:8744–8. [PubMed: 2877461]
10. Oseroff AR, Ara G, Ohuoha D, Aprille J, Bommer JC, Yarmush ML. Strategies for selective cancer photochemotherapy: antibody-targeted and selective carcinoma cell photolysis. Photochem Photobiol. 1987; 46:83–96. [PubMed: 3615636]

11. Mitsunaga M, Ogawa M, Kosaka N, Rosenblum LT, Choyke PL, Kobayashi H. Cancer cell-selective in vivo near infrared photoimmunotherapy targeting specific membrane molecules. Nat Med. 2011; 17:1685–91. [PubMed: 22057348]
12. Mitsunaga M, Nakajima T, Sano K, Kramer-Marek G, Choyke PL, Kobayashi H. Immediate in vivo target-specific cancer cell death after near infrared photoimmunotherapy. BMC Cancer. 2012; 12:345. [PubMed: 22873679]
13. Nakamura Y, Ohler ZW, Householder D, Nagaya T, Sato K, Okuyama S. Near Infrared Photoimmunotherapy in a Transgenic Mouse Model of Spontaneous Epidermal Growth Factor Receptor (EGFR)-expressing Lung Cancer. Mol Cancer Ther. 2017; 16:408–14. [PubMed: 28151706]
14. Nagaya T, Sato K, Harada T, Nakamura Y, Choyke PL, Kobayashi H. Near Infrared Photoimmunotherapy Targeting EGFR Positive Triple Negative Breast Cancer: Optimizing the Conjugate-Light Regimen. PLoS One. 2015; 10:e0136829. [PubMed: 26313651]
15. Nakajima T, Sato K, Hanaoka H, Watanabe R, Harada T, Choyke PL. The effects of conjugate and light dose on photo-immunotherapy induced cytotoxicity. BMC Cancer. 2014; 14:389. [PubMed: 24885589]
16. Sato K, Watanabe R, Hanaoka H, Harada T, Nakajima T, Kim I. Photoimmunotherapy: comparative effectiveness of two monoclonal antibodies targeting the epidermal growth factor receptor. Mol Oncol. 2014; 8:620–32. [PubMed: 24508062]
17. Watanabe R, Hanaoka H, Sato K, Nagaya T, Harada T, Mitsunaga M. Photoimmunotherapy targeting prostate-specific membrane antigen: are antibody fragments as effective as antibodies? J Nucl Med. 2015; 56:140–4. [PubMed: 25500827]
18. Kobayashi H, Choyke PL. Super enhanced permeability and retention (SUPR) effects in tumors following near infrared photoimmunotherapy. Nanoscale. 2016; 8:12504–9. [PubMed: 26443992]
19. Nakamura Y, Bernardo M, Nagaya T, Sato K, Harada T, Choyke PL. MR imaging biomarkers for evaluating therapeutic effects shortly after near infrared photoimmunotherapy. Oncotarget. 2016; 7:17254–64. [PubMed: 26885619]
20. Sano K, Nakajima T, Choyke PL, Kobayashi H. Markedly enhanced permeability and retention effects induced by photo-immunotherapy of tumors. ACS Nano. 2013; 7:717–24. [PubMed: 23214407]
21. Ogawa M, Tomita Y, Nakamura Y, Lee MJ, Lee S, Tomita S. Immunogenic cancer cell death selectively induced by near infrared photoimmunotherapy initiates host tumor immunity. Oncotarget. 2017; 8:10425–36. [PubMed: 28060726]
22. Sato K, Sato N, Xu B, Nakamura Y, Nagaya T, Choyke PL. Spatially selective depletion of tumor-associated regulatory T cells with near-infrared photoimmunotherapy. Sci Transl Med. 2016; 8:352ra110.
23. Ali T, Nakajima T, Sano K, Sato K;Choyke PL, Kobayashi H. Dynamic fluorescent imaging with indocyanine green for monitoring the therapeutic effects of photoimmunotherapy. Contrast Media Mol Imaging. 2014; 9:276–82. [PubMed: 24706611]
24. Nakajima T, Sano K;Mitsunaga M, Choyke PL, Kobayashi H. Real-time monitoring of in vivo acute necrotic cancer cell death induced by near infrared photoimmunotherapy using fluorescence lifetime imaging. Cancer Res. 2012; 72:4622–8. [PubMed: 22800710]
25. Sano K, Mitsunaga M, Nakajima T, Choyke PL, Kobayashi H. Acute cytotoxic effects of photoimmunotherapy assessed by 18F-FDG PET. J Nucl Med. 2013; 54:770–5. [PubMed: 23536226]
26. Gallagher FA, Kettunen MI, Hu DE, Jensen PR, Zandt RI, Karlsson M. Production of hyperpolarized [1,4-13C2]malate from [1,4-13C2]fumarate is a marker of cell necrosis and treatment response in tumors. Proc Natl Acad Sci U S A. 2009; 106:19801–6. [PubMed: 19903889]
27. Witney TH, Kettunen MI, Hu DE, Gallagher FA, Bohndiek SE, Napolitano R. Detecting treatment response in a model of human breast adenocarcinoma using hyperpolarised [1-13C]pyruvate and [1,4-13C2]fumarate. Br J Cancer. 2010; 103:1400–6. [PubMed: 20924379]

28. Howe FA, Robinson SP, McIntyre DJ, Stubbs M, Griffiths JR. Issues in flow and oxygenation dependent contrast (FLOOD) imaging of tumours. NMR Biomed. 2001; 14:497–506. [PubMed: 11746943]
29. Mallidi S, Luke GP, Emelianov S. Photoacoustic imaging in cancer detection, diagnosis, and treatment guidance. Trends Biotechnol. 2011; 29:213–21. [PubMed: 21324541]
30. Taruttis A, van Dam GM, Ntziachristos V. Mesoscopic and macroscopic optoacoustic imaging of cancer. Cancer Res. 2015; 75:1548–59. [PubMed: 25836718]
31. Laufer J, Delpy D, Elwell C, Beard P. Quantitative spatially resolved measurement of tissue chromophore concentrations using photoacoustic spectroscopy: application to the measurement of blood oxygenation and haemoglobin concentration. Phys Med Biol. 2007; 52:141–68. [PubMed: 17183133]
32. Matsumoto S, Saito K, Yasui H, Morris HD, Munasinghe JP, Lizak M. EPR oxygen iimaging and hyperpolarized 13C MRI of pyruvate metabolism as noninvasive biomarkers of tumor treatment response to a glycolysis inhibitor 3-bromopyruvate. Magn Reson Med. 2013; 69:1443–50. [PubMed: 22692861]
33. Nielsen PM, Eldirdiri A;Bertelsen LB;Jorgensen HS, Ardenkjaer-Larsen JH, Laustsen C. Fumarase activity: an in vivo and in vitro biomarker for acute kidney injury. Sci Rep. 2017; 7:40812. [PubMed: 28094329]
34. Day SE, Kettunen MI, Cherukuri MK, Mitchell JB, Lizak MJ, Morris HD. Detecting response of rat C6 glioma tumors to radiotherapy using hyperpolarized [1- 13C]pyruvate and 13C magnetic resonance spectroscopic imaging. Magn Reson Med. 2011; 65:557–63. [PubMed: 21264939]
35. Day SE, Kettunen MI, Gallagher FA, Hu DE, Lerche M, Wolber J. Detecting tumor response to treatment using hyperpolarized 13C magnetic resonance imaging and spectroscopy. Nat Med. 2007; 13:1382–7. [PubMed: 17965722]
36. Gillies RJ, Robey I, Gatenby RA. Causes and consequences of increased glucose metabolism of cancers. J Nucl Med. 2008; 49(Suppl 2):24S–42S. [PubMed: 18523064]
37. Gross S, Gilead A, Scherz A, Neeman M, Salomon Y. Monitoring photodynamic therapy of solid tumors online by BOLD-contrast MRI. Nat Med. 2003; 9:1327–31. [PubMed: 14502284]
38. Liang CP, Nakajima T, Watanabe R, Sato K, Choyke PL, Chen Y. Real-time monitoring of hemodynamic changes in tumor vessels during photoimmunotherapy using optical coherence tomography. J Biomed Opt. 2014; 19:98004. [PubMed: 25253195]
39. Mitsunaga M, Nakajima T, Sano K, Choyke PL, Kobayashi H. Near-infrared theranostic photoimmunotherapy (PIT): repeated exposure of light enhances the effect of immunoconjugate. Bioconjug Chem. 2012; 23:604–9. [PubMed: 22369484]
40. Kishimoto S, Bernardo M, Saito K, Koyasu S, Mitchell JB, Choyke PL. Evaluation of oxygen dependence on in vitro and in vivo cytotoxicity of photoimmunotherapy using IR-700-antibody conjugates. Free Radic Biol Med. 2015; 85:24–32. [PubMed: 25862414]
41. Sato K, Watanabe R, Hanaoka H, Nakajima T, Choyke PL, Kobayashi H. Comparative effectiveness of light emitting diodes (LEDs) and Lasers in near infrared photoimmunotherapy. Oncotarget. 2016; 7:14324–35. [PubMed: 26885688]
42. Sato K, Nakajima T, Choyke PL, Kobayashi H. Selective cell elimination in vitro and in vivo from tissues and tumors using antibodies conjugated with a near infrared phthalocyanine. RSC Adv. 2015; 5:25105–14. [PubMed: 25866624]
43. Nakamura Y, Mochida A, Choyke PL, Kobayashi H. Nanodrug Delivery: Is the Enhanced Permeability and Retention Effect Sufficient for Curing Cancer? Bioconjug Chem. 2016; 27:2225–38. [PubMed: 27547843]

## Highlights

The mechanism of photoimmunotherapy relies on photo-oxidation.

Acute necrotic damage by photoimmunotherapy induces decreased blood flow.

$^{13}$C MR spectroscopy with [1,4]-$^{13}$C fumarate is useful for an early detection of therapeutic effect of photoimmunotherapy.

Serum fumarase can serve as a treatment response biomarker for photoimmunotherapy.

Photoacoustic imaging provides information of real-time hemodynamic change during photoimmunotherapy.

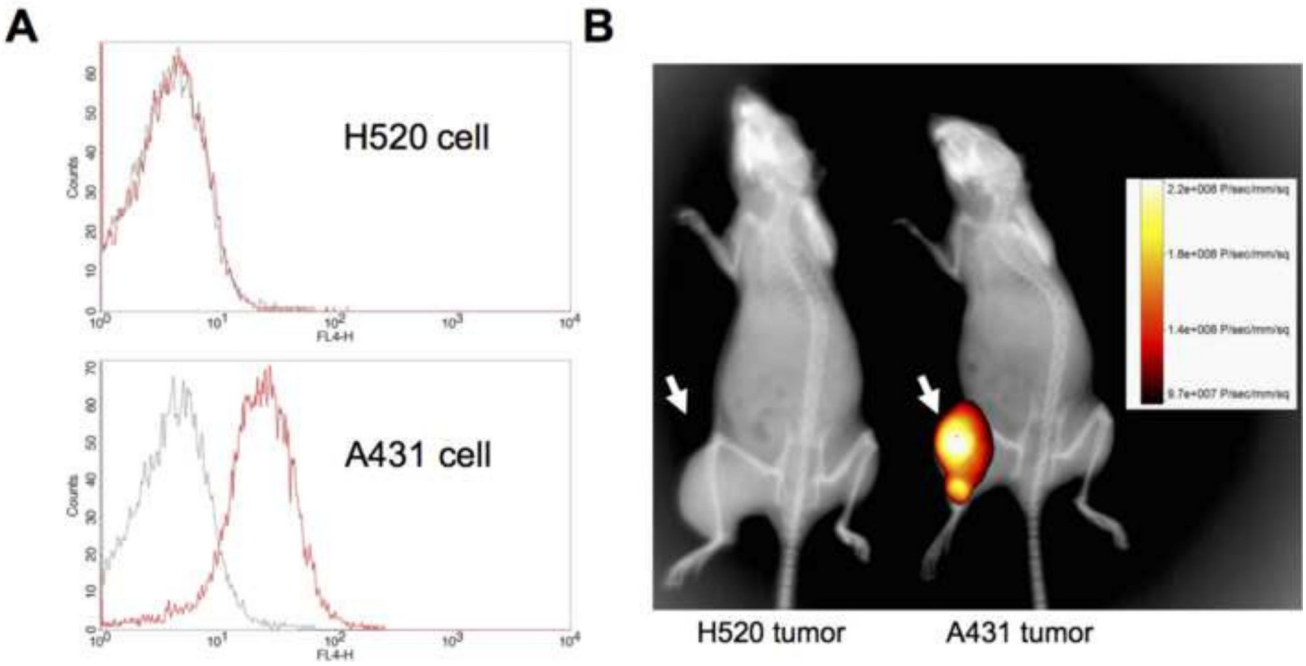


**Figure 1.**

Target accumulation of Pan-IR700 in A431 and H520 cells *in vitro* and *in vivo*. **(A)** A flow cytometry analysis for Pan-IR700 affinity for A431 (top) and H520 (bottom) cells (black line: untreated, red line: Pan-IR700-treated). **(B)** Nude mice implanted with H520 tumors (left) and A431 tumors (right) in the right hind leg were injected with Pan-IR700 24 h prior to fluorescence imaging. Both mice were imaged in the same frame and fluorescence and X-ray modes were simply co-registered.

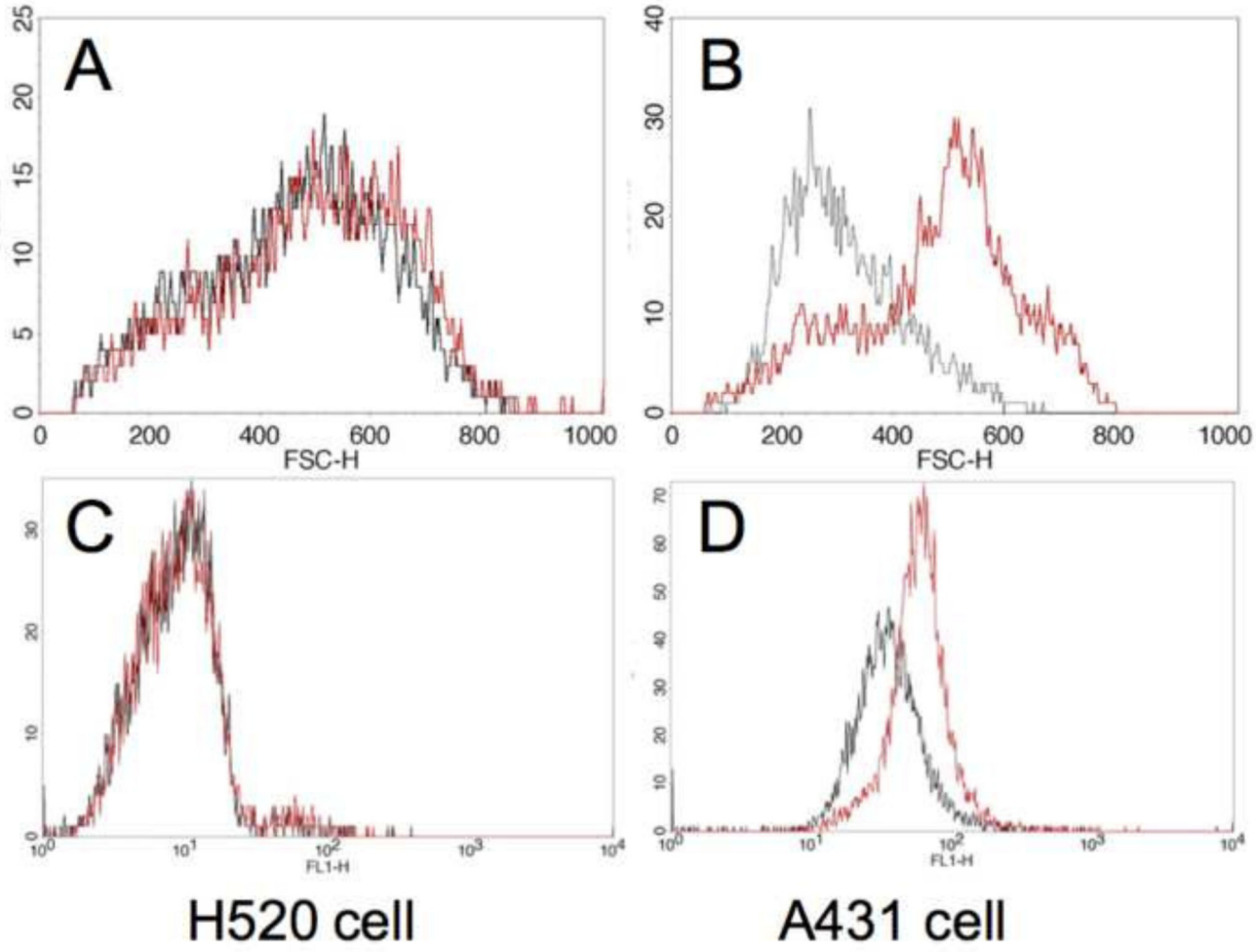


**Figure 2.**

Flow cytometry analysis for oxidative stress. **(A–B)** Forward scatter histograms. **(C–D)** 4-HNE staining histograms. H520 cells (A and C) and A431 cells (B and D) treated with 4-HNE antibody labeled dye were examined by flow cytometry (black line: untreated, red line: NIR PIT-treated). A and B indicate expanded cell size only in NIR PIT-treated A431 cells. C and D indicate that oxidative stress marker 4-HNE is stained only in NIR PIT-treated A431 cells.

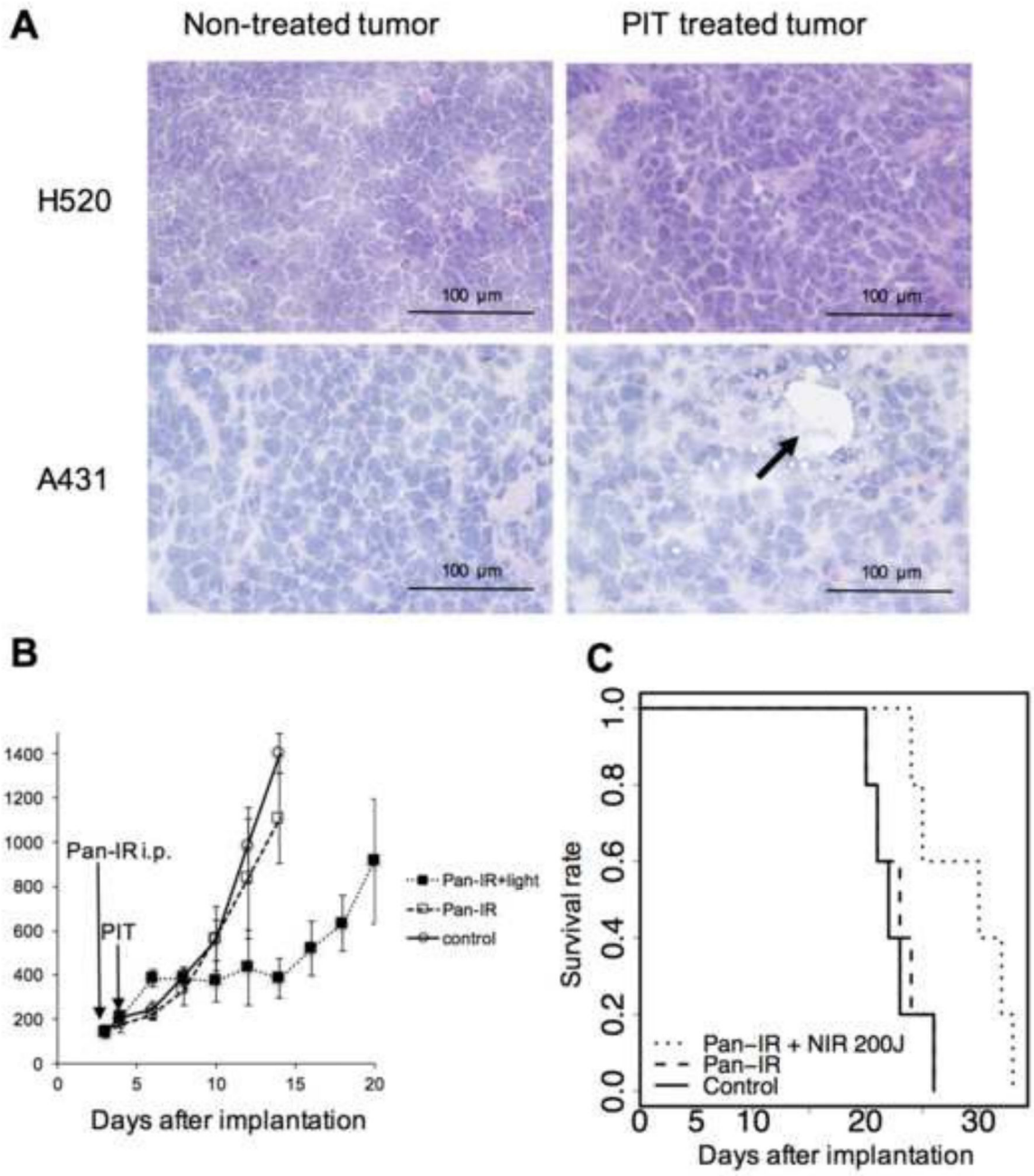


**Figure 3.**

*In vivo* tumoricidal effects of NIR PIT. **(A)** Morphological change in NIR PIT treated tumor cells. Hematoxylin and eosin staining for untreated and NIR PIT treated H520 tumor cells (top row) and untreated and NIR PIT-treated A431 tumor cells (bottom row). Membrane rupture is indicated by the black arrow. **(B)** Tumor growth plot for A431 tumors. Closed squares: Pan-IR700 with NIR PIT (n = 5), open squares: Pan-IR700 only (n = 5), and open circles: no treatment (n = 5). **(C)** Kaplan-Meier survival curve. Solid line: no treatment (control), dashed line: Pan-IR700, and dotted line: Pan-IR700 with NIR PIT. A statistically

significant difference between the control group and the NIR PIT group was observed by a log-rank test ($p = 0.001$).

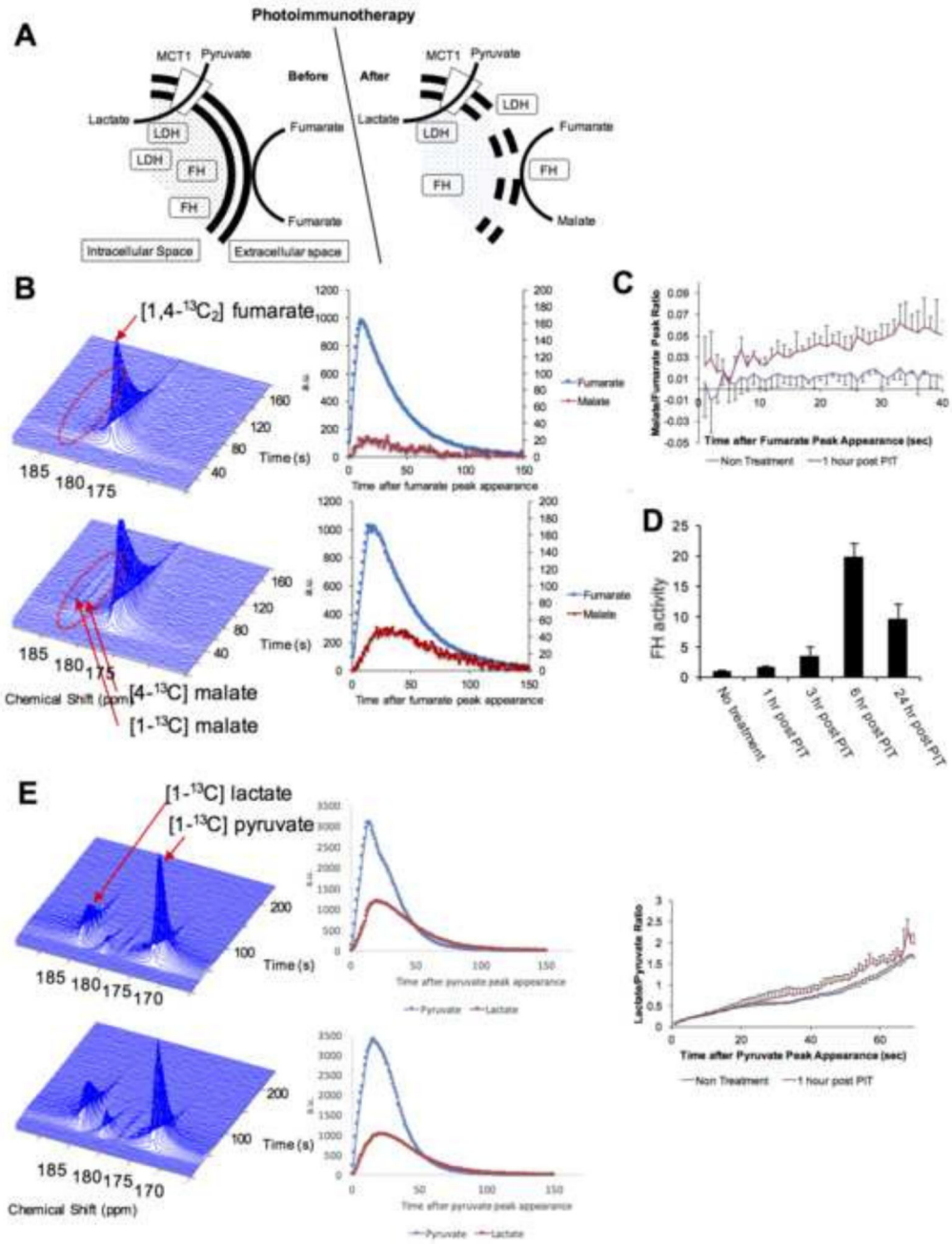


**Figure 4.**

Hyperpolarization $^{13}C$ MRI analysis to detect the tumoricidal effects of NIR PIT. **(A)** Proposed scheme of enzymatic reactions in tumor cells before and after NIR PIT. **(B)** Dynamic spectra of untreated A431 tumors (top, n = 3) and NIR PIT-treated A431 tumors (bottom, n = 4) after hyperpolarized [1,4-$^{13}C_2$] fumarate injection. A malate signal is detected only in NIR PIT-treated tumors. Scatter plots for both fumarate and malate signals are shown at right. **(C)** Plot of malate to fumarate ratio for untreated (black) and NIR PIT-treated (red) A431 tumor cells. **(D)** Trend of serum FH activity after NIR PIT in A431 tumor cells, normalized to the untreated control group (n = 3). **(E)** Dynamic spectra of untreated

(top, n = 4) and NIR PIT-treated (bottom, n = 3) A431 tumors after [1-$^{13}$C] pyruvate injection. Scatter plots for the pyruvate and lactate signals (middle) and the lactate to pyruvate ratio (right) are shown.

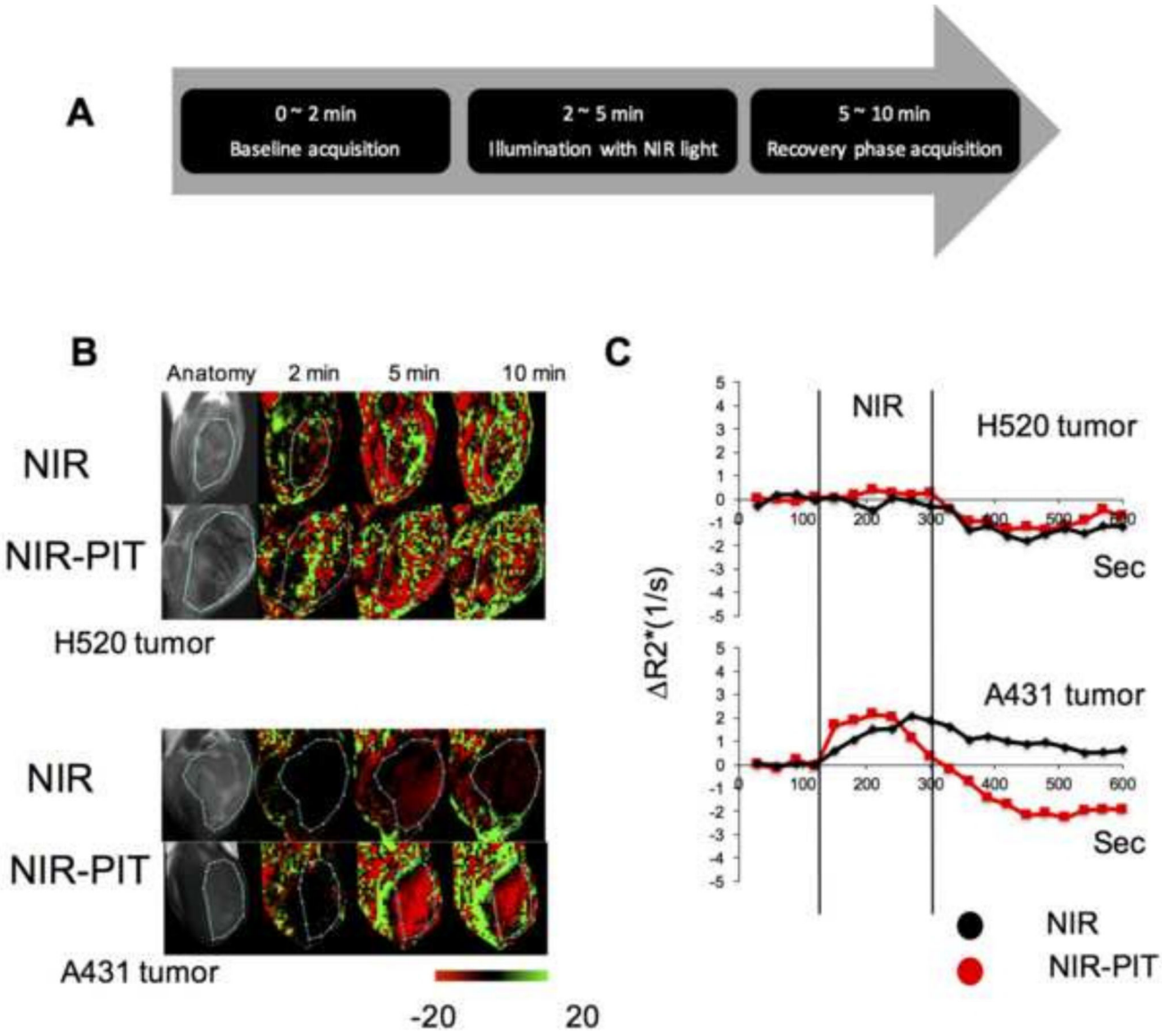


**Figure 5.**

Change in $T_2$*-weighted sequential MRI and $R_2$* during and after NIR PIT. **(A)** Design of the MRI experiment. **(B)** Anatomical image and temporal change in $T_2$*-weighted images for NIR-treated (top rows, n = 6) and Pan-IR700/NIR PIT-treated (bottom rows, n = 5) tumors. Representative images are shown for both H520 (top panel) and A431 (bottom panel) tumors. $T_2$*-weighted images are processed to show the percentage changes (−20% to +20%) from the average image acquired in the baseline scan (0–2 min). **(C)** Plot of change in $R_2$* in tumor area over time. NIR PIT affected the $R_2$* in EGFR-targeted A431 tumor cells but not non-targeted H520 cells.

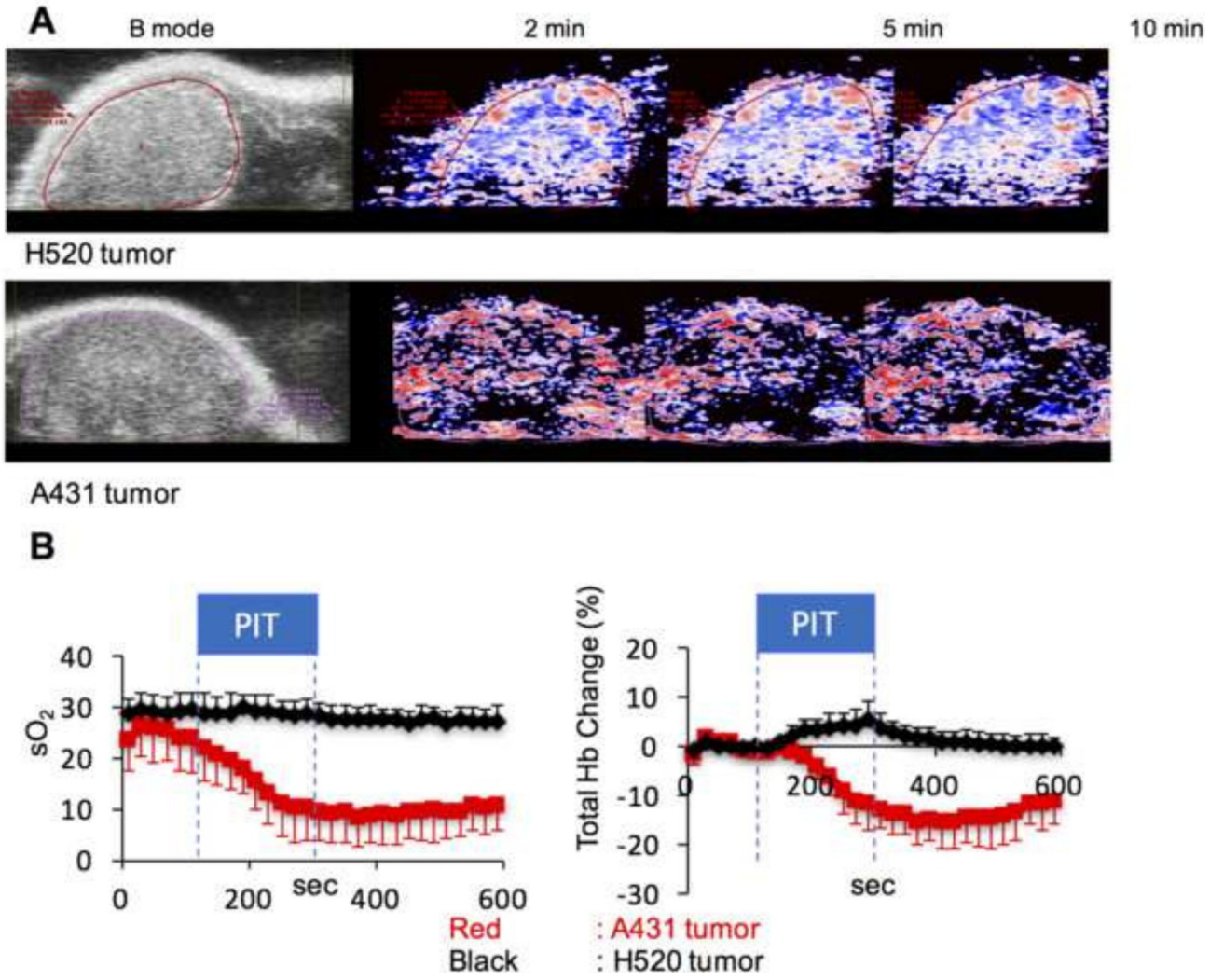


**Figure 6.**

Changes in $sO_2$ and total hemoglobin during and after NIR PIT. **(A)** Anatomical image (B mode) and temporal change in $sO_2$ for NIR PIT-treated H520 (top row, n = 4) and A431 (bottom row, n = 3) tumors. A darkened color map was observed in A431 tumors after NIR PIT treatment. **(B)** Plots of $sO_2$ (left) and total hemoglobin (right) in A431 (red) and H520 (black) tumors. Both $sO_2$ and total hemoglobin values dropped in A431 tumors during NIR PIT, while non-significant changes were observed in H520 tumors.